University of Groningen

Nonconventional morphologies in two-length scale block copolymer systems beyond the weak segregation theory

Kriksin, Yury A.; Erukhimovich, Igor Ya.; Khalatur, Pavel G.; Smirnova, Yuliya G.; ten Brinke, Gerrit

IMPORTANT NOTE: You are advised to consult the publisher's version (publisher's PDF) if you wish to cite from it. Please check the document version below.

Document Version
Publisher's PDF, also known as Version of record

Link to publication in University of Groningen/UMCG research database

Nonconventional morphologies in two-length scale block copolymer systems beyond the weak segregation theory

Yury A. Kriksin,[1] Igor Ya. Erukhimovich,[2] Pavel G. Khalatur,[2,3] Yuliya G. Smirnova,[4] and Gerrit ten Brinke[4,a)]

[1]*Institute for Mathematical Modeling, RAS, Moscow 125047, Russia*
[2]*Institute of Organoelement Compounds, RAS, Moscow 119991, Russia*
[3]*Department of Polymer Science, University of Ulm, Ulm D-89069, Germany*
[4]*Laboratory of Polymer Chemistry, Zernike Institute for Advanced Materials, University of Groningen, Nijenborgh 4, 9747 AG Groningen, The Netherlands*

The order-disorder and order-order transitions (ODT and OOT) in the linear multiblock copolymers with two-length scale architecture $A_{fmN}(B_{N/2}A_{N/2})_n B_{(1-f)mN}$ are studied under intermediate cooling below the ODT critical point where a nonconventional sequence of the OOTs was predicted previously [Smirnova *et al.*, J. Chem. Phys. **124**, 054907 (2006)] within the weak segregation theory (WST). To describe the ordered morphologies appearing in block copolymers (BCs) under cooling, we use the pseudospectral version of the self-consistent field theory (SCFT) with some modifications providing a good convergence speed and a high precision of the solution due to using the Ng iterations [J. Chem. Phys. **61**, 2680 (1974)] and a reasonable choice of the predefined symmetries of the computation cell as well as initial guess for the iterations. The WST predicted sequence of the phase transitions is found to hold if the tails of the BCs under consideration are symmetric enough ($|0.5-f| \leqslant 0.05$); the quantitative agreement between the WST and SCFT phase diagrams is reasonable in a narrow (both in f and $\tilde{\chi} = \chi N$) region close to the critical point, though. For $|0.5-f| > 0.05$, a large region of the face-centered cubic phase stability is found (up to our knowledge, first within the SCFT framework) inside of the body-centered cubic phase stability region. Occurrence of the two-dimensional and three-dimensional phases with the micelles formed, unlike the conventional diblock copolymers, by the longer (rather than shorter) tails, and its relationship to the BC architecture is first described in detail. The calculated spectra of the ordered phases show that nonmonotonous temperature dependence of the secondary peak scattering intensities accompanied by their vanishing and reappearance is rather a rule than exception. © *2008 American Institute of Physics*. [DOI: 10.1063/1.2937138]

I. INTRODUCTION

One of the most interesting phenomena in block copolymer (BC) systems is their self-assembling into ordered morphologies possessing the symmetry of a crystal lattice[1–5] with changing (typically decreasing) temperature T. The physical reason for this self-assembling also called order-disorder transition (ODT) or microphase separation is obvious: With decreasing T the energy gain upon local segregation grows as compared to the loss of the configurational entropy accompanying such segregation, the immiscible blocks being not separated fully because of their covalent bonding. As a result, an ordered pattern of alternating domains filled preferably by monomers of the same sort, i.e., crystal lattice arises. The domains' scale is, naturally, of the order of magnitude of the immiscible block size, i.e., in the range between tens and few hundreds of nanometers, which makes BCs more and more appealing for nano- and nanobiotechnology applications. With further decrease of T, the ODT is often followed by various transitions between the different ordered morphologies (order-order transitions or OOTs). BC melts with different structural and interaction parameters are known to form different morphologies so that the ultimate goal of both theory and experiment is to determine the symmetry and geometry of the most stable ordered phases (as well as the thermodynamic, scattering, and mechanical properties of the phases) for a copolymer melt or blend given its composition, architecture, and temperature.

In most of the BC melts studied in the original papers[6–16] and books,[17–20] the structure formation involves only *one* characteristic length scale. Therewith, the self-assembled phases are generally restricted to the classical lamellar (LAM), hexagonal (HEX), and body-centered cubic (bcc) morphologies first proved to be stable close to the ordering critical point in the seminal weak segregation theory (WST) by Leibler.[6] Later the double gyroid (G) phase possessing the symmetry of the $Ia\bar{3}d$ space group (No. 230) as well as other phases possessing a more complex symmetry were found to be stable not too close to the critical point both experimentally[21,22] and theoretically by Matsen,[12–16] whose so-called self-consistent field theory (SCFT) is free from the WST restriction to a vicinity of the critical point only. Since then the WST has been considered by many authors as a sort of an old-fashioned and outdated technique.

a)Electronic mail: ierukhs@polly.phys.msu.ru.

However, a more thorough comparison[23,24] of the advantages and shortcomings of both the WST and SCFT led us to conclude that even though the SCFT is in many respects superior to the WST beyond the weak segregation realm, application of the SCFT could be considerably facilitated when based on the preliminary WST analysis. Therewith, the most remarkable advantage of the WST is that it provides an express analysis of the architecture dependence of the phase diagrams for rather large families of the BC.[11] In particular, it was demonstrated via such a WST analysis, based on consideration of the architecture dependent structure correlators only,[23–27] that there exist some BC systems, which possess a special architecture giving rise to stability of the complex (nonconventional) morphologies already in a vicinity of the ordering critical point. Remarkably, these special BCs (ternary *ABC* BCs (Refs. 23 and 26) and multiblock *AB* copolymers with a two-length scale architecture described below[24,25,27]) both belong to a newly discovered experimentally[28–33] and theoretically[34–42] class of BC revealing two different spatial length scales. The SCFT analysis of the phase behavior of the linear *ABC* block copolymers has been carried out recently by Morse *et al.*[43,44] There is a noticeable qualitative and even semiquantitative similarity between the WST and SCFT phase diagrams of the linear *ABC* BCs; a substantial difference worth to be mentioned was found in two cases. First, the WST phase diagrams[23,24] do not contain the *Fddd* (orthorhombic) phase stability region found by Morse *et al.*[43,44] This discrepancy is, actually, only due to the fact that the *Fddd* phase has been discovered after the WST phase diagram of the *ABC* BCs had been calculated and, thus, it was simply not included in the list of possible thermodynamically stable phases. Second, the SCFT phase diagrams[16,43,44] do not contain the face-centered cubic (fcc) phase, which is predicted by the WST (Refs. 23–27) to be stable close to and not too far away from the critical ODT point at some values of the parameters. Moreover, Matsen[16] excluded the fcc stability in the ternary *ABC* block copolymers based on some qualitative sphere domain packing considerations (note, however, that the choice of the χ-parameters in Refs. 23, 43, and 44 and Ref. 16 corresponds to different universality classes as discussed in Ref. 23).

In both cases the qualitative discrepancy stems from the necessity to presuppose the possible morphologies, which is a characteristic of any theoretical work. In fact, none of the existing papers could claim that it fully explores all possible candidates to the morphologies expected to be thermodynamically stable: In experiment, we hardly could be completely sure that the observed morphologies do correspond to full thermodynamic equilibrium; in theory we still for long will not be able to explore all 230 3*d* space groups. Even in Refs. 45–47, where the real-space SCFT is used and no *explicit* morphologies are presupposed, the authors assume *implicitly* that there are no stable (or metastable) morphologies but those to which the iteration process does converge starting from a randomly chosen set of the initial inhomogeneities. In other words, all not found morphologies are assumed to be absolutely unstable. However, such an assumption can be proved only via direct testing not found morphologies
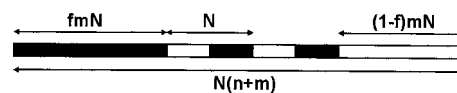

FIG. 1. The architecture of the *AB* multiblock copolymer: n is the number of elementary diblock units forming the middle multiblock part; N is the elementary diblock length; fmN is the length of the tail of A type; $1-fmN$ is the length of the tail of B type.

and, thus, is no more warranted than fixing the explicit list of the presupposed morphologies in advance.

In this paper, we present the SCFT analysis of the phase and morphological behavior of one more class of BC. Namely, we focus on monodisperse melts of macromolecules $A_{fmN}-b-(B_{N/2}-b-A_{N/2})_n-b-B_{(1-f)mN}$ shown schematically in Fig. 1. The total degree of polymerization and the gyration radius of these macromolecules are $N_{tot}=N(n+m)$ and $R_G^2=N_{tot}a^2/6$ (the statistical segment lengths a and excluded volumes ν are assumed to be the same for A and B blocks). Depending on the value of the χ-parameter and the lengths of the "short" diblocks (N), the middle multiblock part as the whole (nN), and the tail blocks [fmN and $(1-f)mN$], self-assembly occurs at either one or two different length scales, which correspond to microphase separation between the long and short blocks and/or inside the $B_{N/2}-b-A_{N/2}$ domains. There is so-called bifurcation region[24,34] in the space of parameters (f,n,m) (see Fig. 2), where fluctuations on both short and long scales are pronounced already in the disordered state. Above the region, the system under consideration first segregates on the large scale, in which case the middle *AB* (black-white) multiblock part behaves as a sort of "gray" block characterized by an average value of the solubility parameter. Accordingly, the phase behavior of such two-scale *AB* multiblock copolymers close to their critical point[24] resembles that of the *ABC* triblock copolymers,[23] whereas further increase of χ could result in additional short-range segregation between the A and B blocks forming the middle (gray) part. We present the phase diagram of the described multiblock copolymers, which is calculated within the pseudospectral version of the SCFT, and compare it to that we calculated previously[24] within the WST. In order not to confuse the comparison, we focus on the nonconventional
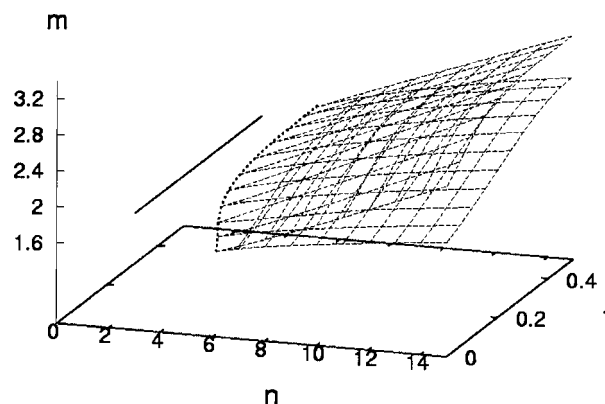

FIG. 2. The dashed wire surface represents the so-called bifurcation surface in the (n,f,m) space. The solid line shows the values of parameters (n,f,m) for the system under investigation.

phase diagrams in that region of the system parameters where segregation inside the middle multiblock part $(B_{N/2} - b - A_{N/2})_n$ *does not occur* yet and, thus, the system phase behavior is somewhat similar to that of the ternary linear *ABC* BCs. (The results of our SCFT analysis of the "lamellar-in-lamellar" effects characteristic of the multiblock *AB* copolymers under study[28,31,32,38,40,48] will be presented elsewhere.) In particular, we confirm that the fcc phase stability region predicted for the considered systems within the WST does remain within the SCFT either.

The paper is organized as follows. The technical details related both to the original SCFT and its modifications in our work are discussed in detail in Sec. II, which could be skipped by the reader not interested directly in this kind of calculations. The results are presented and discussed in Sec. III. Concluding remarks are given in Sec. IV.

II. COMPUTATIONAL METHODOLOGY

A. Brief description of basic numerical methods

There are two strategies that have been applied to solve the SCFT equations: spectral methods[12] and real-space methods.[45–47,49,50] The first strategy is based on the representation of the spatially varying density fields in a Fourier-type basis, using a large number of harmonic terms.[51] The second computational formalism employs an appropriate relaxation (iterative) procedure in order to reach a local minimum of the free energy functional, adjusting simultaneously the chemical potential fields and the conjugate monomer densities at every iteration step. Both schemes have advantages and disadvantages. A disadvantage of the fully spectral schemes is that the computational effort per single iteration scales very poorly (as n_F^3, where n_F is the number of basis functions). Also, it requires that the symmetry of a formed microstructure be specified in advance so that a proper set of harmonic terms can be utilized. The real-space methods do not require the system symmetry in advance but are rather time consuming in three dimensions even on supercomputers. Recent progress in this field has been achieved by using the so-called pseudospectral technique.[52–54] In the context of polymer physics, this technique was first applied by Rasmussen and Kalosakas[53] in order to solve the modified diffusion equation that describes the propagation of monomer densities. Subsequently, Ceniceros and Fredrickson[54] further extended the approach. In particular, they introduced a robust class of semi-implicit numerical methods that employ supplementary information about the nonlocal density operators. As a result, the total computational cost has been reduced by an order of magnitude. Another way to speed up convergence of the SCFT equations for polymeric systems we employ here is to use the iterative scheme by Ng,[55] linearizing the solution around stationary points. A similar (but some technical details we discuss below) procedure was used by Thompson *et al.*[56]

B. The SCFT equations

As described in detail in Refs. 17 and 54 (see also Refs. 35, 38, and 40), the free energy of the incompressible melt of flexible *AB* copolymers reads

$$\mathcal{F}(\{\psi_A\},\{\psi_B\})/T = \int d^3\mathbf{r}[-f_A\psi_A(\mathbf{r}) - (1 - f_A)\psi_B(\mathbf{r}) \\ + (\psi_A(\mathbf{r}) - \psi_B(\mathbf{r}))^2/(4\chi\mathcal{N})] \\ - V\ln Q(\{\psi_A\},\{\psi_B\}). \quad (1)$$

Here V is the system volume; f_A is the average volume fraction of type A blocks $(f_A + f_B = 1)$; $\psi_i(\mathbf{r})$ is the external field acting on the monomer of the ith type located at the point $\mathbf{r}$, the temperature T is measured in the energetic units, in which the Boltzmann constant $k_B = 1$; the *single-chain* partition function Q reads

$$Q(\{\psi_A, \psi_B\}) = V^{-1} \int d^3\mathbf{r} \, q(\mathbf{r}, 1; \{\psi_A, \psi_B\}). \quad (2)$$

The end-to-end distribution function $q(\mathbf{r}, s)$ $\equiv q(\mathbf{r}, s; \{\psi_A, \psi_B\})$ (non-normalized statistical weight) is defined by the modified diffusion equation

$$\partial q(\mathbf{r}, s)/\partial s = R_G^2 \nabla^2 q(\mathbf{r}, s) - \psi(\mathbf{r}, s)q(\mathbf{r}, s), \quad (3)$$

with the initial condition $q(\mathbf{r}, 0) = 1$ and

$$\psi(\mathbf{r}, s) = \sigma_A(s)\psi_A(\mathbf{r}) + \sigma_B(s)\psi_B(\mathbf{r}). \quad (4)$$

Here $\sigma_i(s) = 1$ if the chain contour position s is occupied by the segment of the type i and $\sigma_i(s) = 0$ otherwise.

The desired free energy is the saddle point value of the functional $\mathcal{F}[\psi_A, \psi_B]$ to be obtained via minimization of the latter with respect to the exchange potential

$$\psi_-(\mathbf{r}) = \tfrac{1}{2}[\psi_B(\mathbf{r}) - \psi_A(\mathbf{r})], \quad (5)$$

and maximization with respect to the effective pressure

$$\psi_+(\mathbf{r}) = \tfrac{1}{2}[\psi_B(\mathbf{r}) + \psi_A(\mathbf{r})]. \quad (6)$$

The SCFT equations defining the saddle point fields read[54]

$$\frac{\delta \mathcal{F}}{\partial \psi_+} = \phi_A(\mathbf{r}) + \phi_B(\mathbf{r}) - 1 = 0,$$

$$\frac{\partial \mathcal{F}}{\partial \psi_-} = 2f_A - 1 + \frac{2}{\chi\mathcal{N}}\psi_-(\mathbf{r}) + \phi_B(\mathbf{r}) - \phi_A(\mathbf{r}) = 0, \quad (7)$$

where the local volume fractions $\varphi_A(\mathbf{r})$ and $\varphi_B(\mathbf{r})$ are given by the integrals

$$\phi_i(\mathbf{r}) = Q^{-1}(\{\psi_A, \psi_B\}) \int_0^1 ds\, \sigma_i(s)q(\mathbf{r}, s)\tilde{q}(\mathbf{r}, 1 - s). \quad (8)$$

These equations identify $\varphi_A(\mathbf{r})$ and $\varphi_B(\mathbf{r})$ as the average densities of A and B chain segments at point $\mathbf{r}$ as calculated in an ensemble of noninteracting macromolecules subject to the fields $\psi_A(\mathbf{r})$ and $\psi_B(\mathbf{r})$ acting on A and B segments, respectively. The order parameter of the system is related to the difference between the densities of the two kinds of monomers. The end-segment distribution function $\tilde{q}(\mathbf{r}, s)$, which appears in Eq. (8) and describes the opposite end of a chain (from 1 to 0), is defined similar to Eq. (3):

$$\frac{\partial}{\partial s}\tilde{q}(\mathbf{r},s) = R_G^2 \nabla^2 \tilde{q}(\mathbf{r},s) - \psi(\mathbf{r},1-s)\tilde{q}(\mathbf{r},s), \qquad (9)$$

with $\tilde{q}(\mathbf{r},0)=1$.

C. The Ng procedure

Let us represent Eqs. (1)–(9) as a nonlinear operator equation

$$x = \mathfrak{R}[x], \qquad (10)$$

with $x(\mathbf{r})=[\Psi_+(\mathbf{r}),\Psi_-(\mathbf{r})]$ and

$$\mathfrak{R}[x] = \left(\psi_+ + \frac{\partial \mathcal{F}}{\partial \psi_+} ; \psi_- - \frac{\partial \mathcal{F}}{\partial \psi_-} \right), \qquad (11)$$

where the functional derivatives are defined in Eq. (7) and $\mathfrak{R}$ denotes the corresponding nonlinear operator. The widely used iterative scheme to solve Eq. (10) is based on the Picard-type mixing

$$x^{(t+1/2)} = x^{(t)} + \tau(\mathfrak{R}[x^{(t)}] - x^{(t)}), \qquad (12)$$

followed by a uniform field shift

$$x^{(t+1)} = x^{(t+1/2)} - V^{-1} \int d^3\mathbf{r}\, x^{(t+1/2)}(\mathbf{r}), \quad t=0,1,2,\dots \ . \qquad (13)$$

The iterative scheme (12) and (13) is convergent under proper choice of the mixing parameter τ, which should be sufficiently (as determined empirically) small. Starting with an initial guess $x^{(0)}$, a sequence of output functions $x^{(t)}$ is generated. The fixed point of the sequence (12) and (13) strongly depends on the choice of initial vector $x^{(0)}$ because of multiextremum character of the problem (1)–(9). Generally, the convergence is rather slow. The Ng iterative procedure,[55] which speeds up the convergence substantially, utilizes the input and output iteration functions of several previous iteration steps and hence has a much faster converging rate than the usual (Picard) mixing scheme, especially for difficult cases like copolymers systems at large Flory–Huggins parameters. Namely, a trial input for the $(t+1)$th iteration is given by the linear combination

$$x = x^{(t)} - \sum_k^n \tau_k (x^{(t)} - x^{(t-k)}), \quad k=1,2,\dots,n, \qquad (14)$$

with $n=10$. To find the best possible solution at a current iteration step, we optimize the set $\{\tau_k\}$ by minimizing the norm

$$D(\tau) = \left\{ \sum_{\alpha=A,B} \int d\mathbf{r}(\mathfrak{R}[x(\mathbf{r})] - x(\mathbf{r}))^2 \right\}^{1/2}$$
$$= \left\{ \sum_{\alpha=A,B} \int d\mathbf{r}\left(\delta^{(t)} - (\mathbf{r}) - \sum_k^n \tau_k \Delta_k(\mathbf{r}) \right)^2 \right\}^{1/2}, \qquad (15)$$

with respect to $\{\tau_k\}$. Here $x(\mathbf{r})$ is defined by Eq. (14) and

$$\delta^{(t)} = \mathfrak{R}x^{(t)} - x^{(t)}, \qquad (16)$$

$$\Delta_k = \delta^{(t)} - \delta^{(t-k)} = (\mathfrak{R}[x^{(t)}] - x^{(t)}) - (x^{(t-k+1)} - x^{(t-k)}). \qquad (17)$$

As a result, the set $\{\tau_k\}$ is determined by the simultaneous linear equations

$$\Delta_{11}\tau_1 + \Delta_{12}\tau_2 + \cdots + \Delta_{1n}\tau_n = \delta^{(t1)},$$

$$\Delta_{21}\tau_1 + \Delta_{22}\tau_2 + \cdots + \Delta_{2n}\tau_n = \delta^{(t2)},$$

$$\cdots,$$

$$\Delta_{n1}\tau_1 + \Delta_{n2}\tau_2 + \cdots + \Delta_{nn}\tau_n = \delta^{(tm)}, \qquad (18)$$

where $\Delta_{lm}=\int d\mathbf{r}\Delta_l(\mathbf{r})\Delta_m(\mathbf{r})$ and $\delta^{(tm)}=\int d\mathbf{r}\delta^{(t)}(\mathbf{r})\delta_m(\mathbf{r})$.

Having $\{\tau_k\}$, the input for the next $(t+1)$th iteration is defined as

$$x^{(t+1/2)} = \mathfrak{R}[x^{(t)}] - \sum_{k=1}^n \tau_k(\mathfrak{R}[x^{(t)}] - \mathfrak{R}[x^{(t-k)}]), \qquad (19)$$

with the uniform field shift $x^{(t+1)}=x^{(t+1/2)}-V^{-1}\int d^3\mathbf{r}x^{(t+1/2)}(\mathbf{r})$.

This fast-converging iteration scheme approximates the nonlinear operator $\mathfrak{R}$ by a different linear operator in the neighborhood of $x^{(t)}$ at a given iteration step t. Equation (19) becomes the simple Picard interaction algorithm (12) for $n=1$.

To implement the described iteration scheme and find the (meta)stable periodic morphologies, the following steps are to be done: (i) starting with some trial functions $\psi_\alpha(\mathbf{r})$ and initial conditions $q_\alpha(\mathbf{r},0)$ and $\tilde{q}_\alpha(\mathbf{r},0)$, to solve the diffusion Eqs. (3) and (9) with periodic boundary conditions prescribed by the choice of the computational cell (see below); (ii) with the solutions from step (i), to generate the single-chain partition function Q via Eq. (2); (iii) with the results of these two steps, to calculate the volume fractions $\varphi_\alpha(\mathbf{r})$'s via Eq. (8) and new self-consistent potentials $\psi_\alpha(\mathbf{r})$ via Eqs. (5)–(7) to be used for the next iteration; (iv) to minimize the free energy functional (1) with respect to the parameters of chosen computational cell.

The stop criterion for the iterations is $\max|\mathfrak{R}[x(\mathbf{r})] - x(\mathbf{r})| < \varepsilon$, $|x(\mathbf{r})|^2 = (\psi_+(\mathbf{r}))^2 + (\psi_-(\mathbf{r}))^2$. For $\varepsilon=10^{-5}$, which corresponds to the error $\sim 10^{-10}$ in Eq. (11) of Ref. 56, the number of iterations necessary to achieve the stop criterion for the standard diblock copolymer model is practically the same as that obtained by Thompson *et al.*[56] (see Tables I and II in Ref. 56) via somewhat different version of the Ng procedure (Anderson mixing), which corresponds to setting $n=3$ in Eq. (19). However, in this paper, we are to deal with the eight-block (two tails and three diblocks in the middle) copolymer melt, which causes a considerable slowing down as well as the accuracy deterioration. For moderately segregated three-dimensional (3D) morphologies formed in this case, the convergence of the Ng iterative scheme is two orders of magnitude faster than that of the Picard one, which is considerably better than the results reported in Ref. 56.

D. The pseudospectral algorithm

Solving the diffusion equations is the most expensive step in the calculation. With a pseudospectral algorithm

stemming from quantum dynamics,[52] Eq. (3) is integrated forward in s from the initial condition at $s=0$ to $s=1$:

$$q(\mathbf{r},s+\Delta s) = \exp(-\psi(\mathbf{r},s)\Delta s/2)\exp(\Delta s\nabla^2)$$
$$\times \exp(-\psi(\mathbf{r},s)\Delta s/2)q_\alpha(\mathbf{r},s) + O((\Delta s)^3). \quad (20)$$

The "bracket" operator $\exp(-\psi(\mathbf{r},s)\Delta s/2)$ appearing in Eq. (20) is applied in the real space, while the operator $\exp(\Delta s\nabla^2)$ is applied in the reciprocal space via the fast Fourier transform (FFT). More precisely, the computation procedure consists of the following steps: starting from $q(\mathbf{r},0)=1$, (i) to evaluate the product $U(\mathbf{r},s,\Delta s)$ $=\exp(-\psi(\mathbf{r},s)\Delta s/2)q(\mathbf{r},s)$ for each $\mathbf{r}$ in the direct space; (ii) to calculate the Fourier transform $U_\mathbf{k}$ $=\int U(\mathbf{r},s,\Delta s)\exp(i\mathbf{kr})d\mathbf{r}$, apply to $U_\mathbf{k}$ in reciprocal space the operator $\exp(\Delta s\nabla^2)$ and calculate the inverse Fourier transform of the result $\bar{U}(\mathbf{r},s,\Delta s)$; (iii) to find $q(\mathbf{r},s+\Delta s)$ $=\exp(-\psi(\mathbf{r},s)\Delta s/2)\bar{U}(\mathbf{r},s,\Delta s)$ and return to step (i). Thereby, one should have in mind that, as consistent with definition (4), the field $\psi(\mathbf{r},s)$ as a function of s is continuous only within $2n$ intervals (s_k,s_{k+1}) ($s_0=0$ and $s_{2n+2}=1$ are the chain ends) and have discontinuity in $2n+1$ points $\{s_k\}$ corresponding to the boundaries between A and B blocks. The same scheme is used to integrate Eq. (9). In both cases, we use the periodic boundary conditions.

There are two important aspects in the scheme outlined above. First, the solution of the SCFT equations is, obviously, not unique (several metastable morphologies could exist). So, both the convergence of the iteration and the resulting morphologies strongly depend on the initial guess $x^{(0)}$ $=[\Psi_+^{(0)}(\mathbf{r}),\Psi_-^{(0)}(\mathbf{r})]$. Often the initial values of the fields are randomly generated.[57] Instead, in this paper, we use for the initial guesses an information on the symmetry of the plausible morphologies provided by the WST (see below). Second, if the type of expected symmetry is known in advance or can be guessed or predicted, it is natural to choose the computational cell and initial fields fitting this symmetry. Traditionally, the SCFT-based calculations in real space use only the Cartesian coordinates rather than the crystallographic ones. However, our preliminary studies revealed that an appropriate choice of the computational cell symmetry system could result in the better convergence.

E. The computation cell

A triclinic (in general) basis of the cell $\{\mathbf{t}_1,\mathbf{t}_2,\mathbf{t}_3\}$ defines the set of the translation vectors $\mathbf{T_k}=k_1\mathbf{t}_1+k_2\mathbf{t}_2+k_3\mathbf{t}_3$, $\mathbf{k}$ $=(k_1,k_2,k_3)$ being an integer vector. So, the equalities $\psi_\alpha(\mathbf{r}+\mathbf{T_k})=\psi_\alpha(\mathbf{r})$, $q(\mathbf{r}+\mathbf{T_k},s)=q(\mathbf{r},s)$, etc., hold. Requirement of a space group symmetry for the morphology under study implies that the corresponding functions $\psi_+^{(0)}(\mathbf{r})$ and $\psi_-^{(0)}(\mathbf{r})$ have the Fourier expansions

$$\psi_\pm^{(0)}(\mathbf{r}) = \sum_{\{m\}} A_m \exp[i(\mathbf{q}_m \cdot \mathbf{r} + \phi_m)], \quad (21)$$

where A_m and ϕ_m are the amplitudes and phases, respectively, $A_m = A_{-m}$, $\phi_{-m} = -\phi_m$ since the functions $\psi_\pm^{(0)}(\mathbf{r})$ are

real, $\{\mathbf{m}\}$ is the set of the vectors $\mathbf{m}=(m_1,m_2,m_3)$ with integer m_i and the wave vectors $\mathbf{q}_m$ read

$$\mathbf{q}_m = 2\pi(m_1\mathbf{g}_1 + m_2\mathbf{g}_2 + m_3\mathbf{g}_3), \quad (22)$$

where the vector triple $\{\mathbf{g}_1,\mathbf{g}_2,\mathbf{g}_3\}$ is the reciprocal basis for the chosen cell basis $\{\mathbf{t}_1,\mathbf{t}_2,\mathbf{t}_3\}$:

$$\mathbf{t}_l \cdot \mathbf{g}_m = \delta_{lm} \quad (l,m=1,2,3). \quad (23)$$

The sum in definition (21) is assumed only over those vectors $\mathbf{q}_m$, which belong to the chosen reciprocal lattice.[58] The symmetry of the space group is conveyed to the $\psi_\pm^{(0)}(\mathbf{r})$ functions through the sets of the allowed $\{\mathbf{q}_m\}$ (the choice of the reciprocal lattice) and phase shifts $\{\phi_m\}$. A triclinic computational cell is characterized by three edge lengths, $D_l=|\mathbf{t}_l|$, and three angles, θ_{lm}, between the vectors $\mathbf{t}_l$ and $\mathbf{t}_m$. In general, the free energy functional (1) depends both on D_l and θ_{lm} so that these parameters are to be obtained via minimization of $\mathcal{F}[\psi_A,\psi_B]$ (obviously, the saddle point solution is to be recalculated for every change of the set $\{\mathbf{D};\boldsymbol{\theta}\}$).

In our calculations, we are using the rectangular basis

$$\mathbf{t}_i \cdot \mathbf{t}_j = D^2 c_i \delta_{ij}, \quad i,j=1,2,3 \quad (24)$$

(the case $c_1=c_2=c_3=1$ corresponds to the cubic symmetry, $c_3=1$, $c_2=1/\sqrt{3}$, $c_1=c_2/2$ does to the orthorhombic *Fddd* morphology), the hexagonal basis,

$$\mathbf{t}_l^2 = D^2, \quad \mathbf{t}_1 \cdot \mathbf{t}_2 = D^2/2, \quad \mathbf{t}_1 \cdot \mathbf{t}_3 = \mathbf{t}_2 \cdot \mathbf{t}_3 = 0, \quad (25)$$

and the rhombohedric basis,

$$\mathbf{t}_l \cdot \mathbf{t}_m = (D^2/2)(1+\delta_{lm}), \quad l,m=1,2,3. \quad (26)$$

The free energy (1) is to be minimized with respect to the periodicity D, as shown in Ref. 59.

For a triclinic basis application of the Laplace operator ∇^2 in the Fourier space requires some accuracy. Indeed, for an arbitrary value of $\mathbf{q}=q_1\mathbf{g}_1+q_2\mathbf{g}_2+q_2\mathbf{g}_2$, the action of the Laplacian $\nabla^2=(\mathbf{e}_1\partial/\partial x_1+\mathbf{e}_2\partial/\partial x_2+\mathbf{e}_3\partial/\partial x_3)^2$ and the operator $\exp(\Delta s\nabla^2)$ to a harmonic wave $\exp(i\mathbf{q}\cdot\mathbf{r})$ is, respectively, just multiplication by a factor

$$\nabla^2 \exp(i\mathbf{q}\cdot\mathbf{r}) = C \exp(i\mathbf{q}\cdot\mathbf{r}), \quad (27)$$

$$\exp(s\nabla^2)\exp(i\mathbf{q}\cdot\mathbf{r}) = C_E \exp(i\mathbf{q}\cdot\mathbf{r}), \quad C_E = \exp(C\Delta s), \quad (28)$$

where $C=-\sum_{n=1}^3(\sum_{k=1}^3 g_{kn}q_k)^2$ and $g_{kn}=\mathbf{g}_k\cdot\mathbf{e}_n$.

Now, any periodic function $u(\mathbf{r})$ defined in the computational cell can be written as a Fourier series expansion,

$$u(\mathbf{r}) = \sum_m U_m \exp(i\mathbf{q}_m\cdot\mathbf{r}), \quad \mathbf{m}=(m_1,m_2,m_3), \quad (29)$$

with

$$U_m = V^{-1}\int d^3\mathbf{r}\,u(\mathbf{r})\exp(-i\mathbf{q}_m\cdot\mathbf{r}). \quad (30)$$

The coefficients U_m can be approximated as follows:

$$U_m \approx \bar{U}_m = (L_1 L_2 L_3)^{-1} \sum_1 u(\mathbf{r}_1) \exp(-i\mathbf{q}_m \cdot \mathbf{r}_1)$$

$$= (L_1 L_2 L_3)^{-1} \sum_1 u(\mathbf{r}_1) \exp\left(-2\pi i \sum_{i=1}^{3} m_i l_i / L_i\right), \quad (31)$$

where $\mathbf{l} = (l_1, l_2, l_3)$ is the non-negative integer vector ($l_\tau = 0, 1, 2, \ldots, L_\tau - 1$; $\tau = 1, 2, 3$) and

$$\mathbf{r_l} = \sum_{i=1}^{3} l_i \mathbf{t}_i / L_i. \quad (32)$$

The sum in the rhs of Eq. (31) is the discrete Fourier transform (DFT) of $u(\mathbf{r}_l)$ that depends on discrete argument $\mathbf{r}_l$. If all values of $\tilde{U}_m$ are known, it is possible to restore $u(\mathbf{r}_l)$ via inverse DFT:

$$u(\mathbf{r_l}) = \sum_m \tilde{U}_m \exp\left(-2\pi i \sum_{i=1}^{3} m_i l_i / L_i\right), \quad (33)$$

where $m_\tau = 0, 1, 2, \ldots, L_\tau - 1$; $\tau = 1, 2, 3$. It should be noted that the discrete functions U_m and $\tilde{U}_m$ are essentially different. The former is periodic with the periods L_1, L_2, L_3. The latter is an infinite-dimensional vector. The approximate equality between them takes place only for small enough values of $|\mathbf{m}|$. If $u(\mathbf{r})$ is a real function, we have

$$U_{-m} = (U_m)^*, \quad \tilde{U}_{-m} = (\tilde{U}_m)^*, \quad (34)$$

where $*$ denotes the complex conjugation.

Application of the operator $\exp(\Delta s \nabla^2)$ to the values of $\tilde{U}_m$ is not trivial. There is a typical mistake when one simply multiplies $\tilde{U}_m$ by C_E defined by Eq. (28), which is correct for the Fourier coefficients U_m but not for $\tilde{U}_m$, which are to satisfy the periodic conditions

$$\tilde{U}_{m+T} = \tilde{U}_m, \quad (35)$$

$$\mathbf{T} = (k_1 L_1, k_2 L_2, k_3 L_3), \quad k_\tau = 0, \pm 1, \pm 2, \ldots. \quad (36)$$

Indeed, the product $C_E \tilde{U}_m$ does not satisfy these conditions and, as a result, the inverse DFT of $C_E \tilde{U}_m$ is a complex value. Due to the presence of nonzero imaginary part, it contains additional errors. Hence, the multiplier C_E in Eq. (28) should be properly modified to avoid the nonphysical imaginary part in the result. The simplest and effective way we suggest is to replace C_E by the function

$$\tilde{C}_E(\mathbf{m}) = \begin{cases} C_E(\mathbf{m}), & |m_\tau| < L_\tau/2 \\ C_E(\mathbf{m} + \mathbf{T}), & |m_\tau + k_\tau L_\tau| < L_\tau/2 \\ 0, & |m_\tau + k_\tau L_\tau| = L_\tau/2, \end{cases} \quad (37)$$

where $\mathbf{T}$ is given by Eq. (36) and the vectors $\mathbf{m}$ and $\mathbf{q}$ are interrelated by Eq. (22).

Several points concerning the described modification of the pseudospectral method are worth noting. First, thanks to using the function (37) instead of Eq. (28), the discrete approximation $\tilde{C}_E \tilde{U}_m$ of the Fourier transform $\exp(\Delta s \nabla^2) u(\mathbf{r})$, which is to be calculated when the diffusion Eqs. (3) and (9) are solved, is always a real value in the direct space and

thereby provides a good accuracy for the amplitudes of low harmonics $\exp(i\mathbf{q}_m \cdot \mathbf{r})$ in Eq. (21). (A similar procedure for the orthonormal basis is described by Fredrickson.[17]) Second, when the Fourier spectrum of the solution of the modified diffusion equation is represented by the low-frequency harmonics, the pseudospectral method provides high accuracy even for rather rough grid used in Eq. (31). The point is that the discrete approximation (37) of the operator $\exp(\Delta s \nabla^2)$ corresponds exactly to its representation (28) in reciprocal space just for low frequencies.

F. The weak segregation theory and initial guess

In this paper, we use for the initial guesses that information on the plausible morphologies, which is provided by the WST. The latter could be derived from an alternative formulation of the self-consistent field approximation, in which the master quantity is the free energy Ξ of the BC system under consideration as a functional of the spatial distribution of the actual densities (numbers per unit volume) of the monomers of the ith sort $\rho_i(\mathbf{r})$, the equilibrium density distribution $\bar{\rho}_j(\mathbf{r})$ being provided via minimization of Ξ:

$$\min \Xi(\{\rho_A(\mathbf{r}), \rho_B(\mathbf{r})\}) = \Xi(\{\bar{\rho}_A(\mathbf{r}), \bar{\rho}_B(\mathbf{r})\}). \quad (38)$$

The Landau expansion of Ξ in powers of the fluctuations $\Delta_i(\mathbf{r}) = \rho_i(\mathbf{r}) - \bar{\rho}_i$ is

$$\Xi(\{\Delta_i(\mathbf{r})\}) = \Xi(\{\bar{\rho}_i\}) + \sum_{n=2}^{4} \frac{1}{n!} \int \Gamma_{i_1, \ldots, i_n}^{(n)}$$

$$\times (\mathbf{r}_1 - \mathbf{r}, \ldots, \mathbf{r}_n - \mathbf{r}) \prod_{i=1}^{n} \Delta_i(\mathbf{r}_i) d\mathbf{r}_i, \quad (39)$$

where the kernels $\Gamma_{i_1, \ldots, i_n}^{(n)}(\mathbf{r}_1 - \mathbf{r}, \ldots, \mathbf{r}_n - \mathbf{r})$ are expressed in terms of structural many-point correlators of the Gaussian chains first introduced and calculated for diblock copolymers by Leibler[6] (other architectures are considered, e.g., in Refs. 10, 11, 24, and 25). In the Fourier transform, the free energy (39) for binary AB incompressible systems reads

$$\Xi = \Xi(\{\bar{\rho}_i\}) + \frac{1}{2} \int \Gamma_2(q) |\Delta(\mathbf{q})|^2$$

$$+ \sum_{n=3,4} \frac{1}{n!} \int \delta\left(\sum_{i=1}^{n} \mathbf{q}_i\right) \Gamma_n(\mathbf{q}_1, \ldots, \mathbf{q}_n) \prod_{i=1}^{n} \frac{\Delta(\mathbf{q}_i) d\mathbf{q}_i}{(2\pi)^3}. \quad (40)$$

Here $\nu \Delta(\mathbf{q}) = (1/2) \int d\mathbf{r} (\varphi_A(\mathbf{r}) - \varphi_B(\mathbf{r})) \exp(i\mathbf{q}\mathbf{r})$ and

$$\Gamma_2(q) = \tilde{g}^{-1}(q) - 2\chi, \quad (41)$$

where the function $\tilde{g}^{-1}(q)$ depends on the BC architecture only and has a minimum at $q = q^* > 0$. Thus, the loss of the spatially homogeneous state stability [positive definiteness of the quadratic term in the expansion (40)] takes place at $\chi > \chi_c = \tilde{g}^{-1}(q^*)$ for the composition harmonic waves with the wave numbers close to $q = q^*$. As a result, the symmetry of the uniform phase gets broken and the composition profile $\Delta(\mathbf{r})$ acquires a space group symmetry:

$$\Delta(\mathbf{r}) = A \sum_{|q_m = q^*|} \exp[i(\mathbf{q}_m \cdot \mathbf{r} + \phi_m)]. \tag{42}$$

Unlike the general expression (21), expansion (42) is only an approximation ("the first harmonics approximation") since summation in Eq. (42) is only over those wave vectors, which belong to the first coordination sphere of the chosen reciprocal lattice. Substituting Eqs. (41) and (42) into Eq. (40) results in the following simple expression for the free energy of the weakly segregated morphology corresponding to the space group (morphology) $\mathfrak{R}$:

$$\Xi_{\mathcal{R}} = \Xi_{\mathcal{R}}(\{\bar{\rho}_i\}) + \min F_{\mathcal{R}}(A),$$
$$F_{\mathcal{R}}(A) = \tau A^2 + \gamma C_{\mathcal{R}} A^3 + \beta_{\mathcal{R}} A^4. \tag{43}$$

Here $\tau = \chi_c - \chi$ is the reduced temperature, A is a reduced order parameter amplitude, the procedure to calculate the structure-dependent material constant γ, the symmetry-dependent factor $C_{\mathfrak{R}}$, and the factor $\beta_{\mathfrak{R}}$, which is determined both by the architecture and symmetry, is described in detail in Refs. 6, 10, 11, 23, 24, and 60). Finding the minimal of the free energies (43) for various $\mathfrak{R}$, one gets the most thermodynamically stable morphology $\bar{\mathfrak{R}}$ and, as a by-product, the composition spatial profile (42) for $\bar{\mathfrak{R}}$. Besides, one can find easily the phase transition lines

$$\tau = \tau_{\mathcal{R}_1 \mathcal{R}_2}(\gamma), \tag{44}$$

where the two morphologies $\mathfrak{R}_1$ and $\mathfrak{R}_2$ simultaneously have the same minimal free energy. Even though the WST applicability could be justified only in a vicinity of the critical point, where the parameter γ appearing in the definition (43) vanishes, it provides semiquantitative but reasonable results within a considerable region of the system parameters around the critical point.

Now, to choose the proper initial guess for the SCFT equations, let us return to Eqs. (7) and (8), which relate the exchange potential $\psi_-(\mathbf{r})$ defined by Eq. (5) to the local order scalar parameter

$$\Phi(\mathbf{r}) = \{(\varphi_A(r) - f_A) - (\varphi_B(r) - f_B)\}/2 = v\Delta(\mathbf{r}) \tag{45}$$

as follows:

$$\psi_-(\mathbf{r}) = \chi N \Phi(\mathbf{r}). \tag{46}$$

In other words, the exchange potential and order parameter have the same symmetry and the choice of the initial distribution of the former basically predetermines the symmetry of the latter whereas the pressure field $\psi_+^{(0)}(\mathbf{r})$ does not influence it at all. So, it is natural to choose the computational cell to be consistent with the symmetry $\mathfrak{R}$ under study and the initial iteration as follows:

$$\psi_+^{(0)}(\mathbf{r}) = 0, \tag{47}$$

$$\psi_-^{(0)}(\mathbf{r}) = A \sum_{|q_m| = q^*} \exp[i((\mathbf{q}_m, \mathbf{r}) + \phi_m)], \quad A = \text{const} > 0. \tag{48}$$

For 3D morphologies, the initial guess (47) and (48) provides approximately three times faster convergence than that
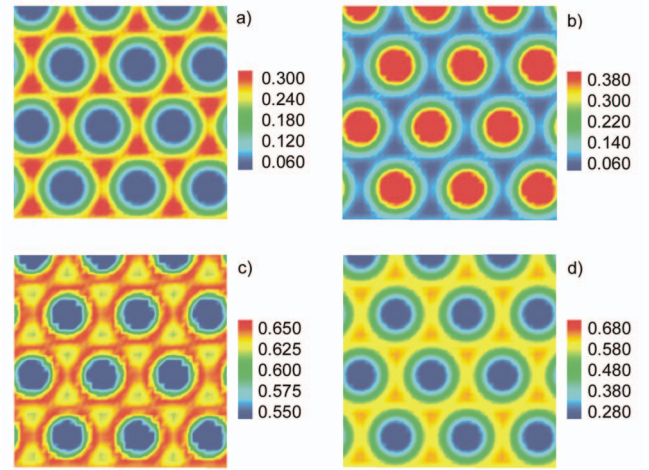

FIG. 3. (Color) The 2D visualization of the inverse HEX morphology at the triple point 1 (see the phase diagram plotted in Fig. 8): [(a) and (b)] distributions of the volume fraction $\varphi_A^{\text{tail}}(\mathbf{r})$ ($\varphi_B^{\text{tail}}(\mathbf{r})$) of the monomers $A(B)$ belonging to the tails $A(B)$ only; (c) distribution of the volume fraction $\varphi_{\text{middle}}(\mathbf{r})$ of those monomers A and B that belong to the multiblock middle part only; (d) distribution of the total volume fraction $\varphi_A(\mathbf{r})$ of all monomers A. The red and blue colors correspond to the maxima and minima, respectively, of the pictured volume fraction.

for a typical random initial field $\psi_-^{(0)}(\mathbf{r})$, which is a considerable gain (especially having in mind slowing down of the SCFT numerical procedure for the eight-block copolymer melt under study) of the same order of magnitude as that due to Anderson mixing.[56] Remarkably, the initial guess (48) with the properly defined angles ϕ_m (see, e.g., Refs. 23 and 60), which keeps information only on the symmetry of the first coordination sphere of the reciprocal lattice, is sufficient to reproduce (through the subsequent iterations) all the higher harmonics with the correct extinction rules.[58]

III. RESULTS AND DISCUSSION

A. Inversed morphologies

The first peculiarity of the multiblock copolymer melt ($n=3$, $m=2$) studied in this paper is that its set of stable morphologies differs from that of the diblock copolymer melt where the long and short blocks form the matrix and micelles, respectively (we refer to such morphology as "direct"). As is clearly demonstrated by the various volume fractions' profiles[61] shown for two hexagonal morphologies with different degrees of segregation in Figs. 3 and 4 and for the bcc morphology in Fig. 5, in our case the longer end block B segregates into the micelles whereas the shorter one A and the middle multiblock part form together the matrix. Further we refer to such morphologies as the "inversed" ones. It is worth to notice that their counterparts for the ternary ABC linear BC are called core-shell morphologies. [Indeed, it is seen from Figs. 3, 4, and 5(c) that the middle multiblock part forms a sort of shell around the micelles B.]

Both the physical and mathematical reasons for the inversed morphologies to exist are easily understood within the WST framework. Indeed, at the very onset of ordering, its driving force is incompatibility between the longer block and the rest of the multiblock macromolecule, the former being the minority as compared to the latter and, thus, forming the
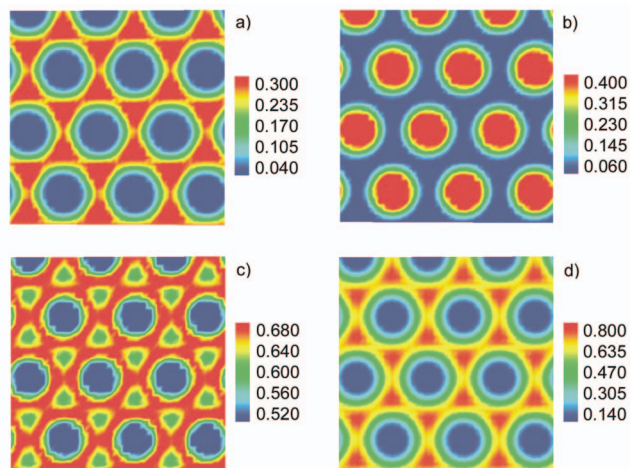
FIG. 4. (Color) The 2D visualization of the inverse HEX morphology at the triple point 2. The legend is the same as in Fig. 3 but the particular values of the corresponding volume fractions assigned to the limiting colors.

micelles. It is also instructive to demonstrate how the microscopic structure of the system is indicating which sort of morphologies, direct or inversed, occurs in the system.

For this purpose, we start with the hexagonal phase, for which the conventional order parameter profile reads

$$\Delta(\mathbf{r}) = A_0 \sum_{i=1,2,3} (\exp(2\pi i(\mathbf{g}_i \mathbf{r} + \phi_i)) + \text{c.c.}), \quad A_0 > 0,$$

(49)

where the vectors $\mathbf{g}_1, \mathbf{g}_2$ being related by Eq. (23) to the translation vectors $\mathbf{t}_1, \mathbf{t}_2$ defined by Eq. (25) and $\mathbf{g}_1 + \mathbf{g}_2 + \mathbf{g}_3 = 0$. A translation $\mathbf{r} \to \mathbf{r} - c_1 \mathbf{t}_1 - c_2 \mathbf{t}_2$ with properly adjusted c_1, c_2 provides elimination of two phases ϕ_1, ϕ_2 so that the only phase ϕ_3 stays not fixed yet. One can check readily that the minimal free energy (43) is achieved at (i) $\phi_3 = 0$, $C_{\Re} = 1$, if $\gamma < 0$ and (ii) $\phi_3 = \pi$, $C_{\Re} = -1$ if $\gamma > 0$.

Thus, in the BCs with an architecture stipulating negativity of γ, the order parameter (43) has maxima $\Delta_{\max} = 6A_0$ and minima $\Delta_{\min} = -3A_0$, which corresponds to the micelles A, whereas in those stipulating positivity of γ the order pa-
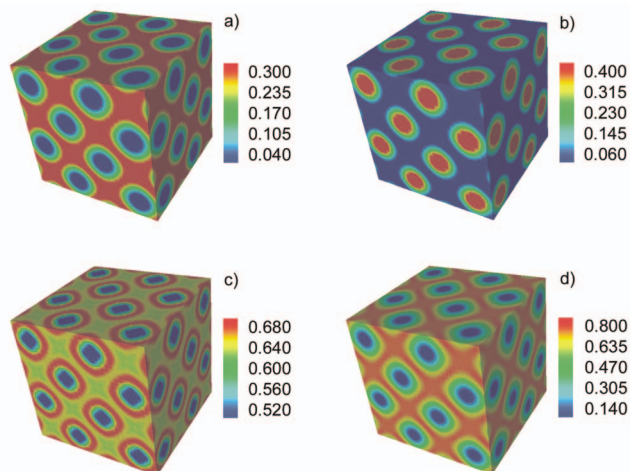

FIG. 5. (Color) The 3D visualization of the inverse bcc morphology at the triple point 4. The legend is the same as in Fig. 3 but the particular values of the corresponding volume fractions assigned to the limiting colors.
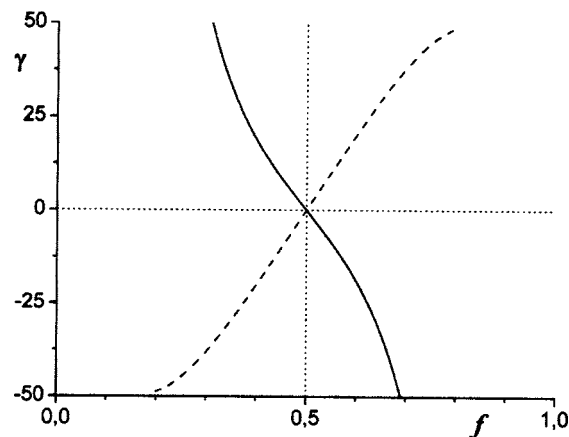

FIG. 6. Plot of the third order vertex function (normalized by the system volume) vs asymmetry parameter f for the diblock (dashed line) and multiblock with $n=3$ and $m=2$ (solid line).

rameter has maxima $\Delta_{\max} = 3A_0$ and minima $\Delta_{\min} = -6A_0$, which corresponds to the micelles B. If γ changes its sign then a reversion of the micelles and matrix occurs. As shown in Fig. 6, the dependences $\gamma(f)$ calculated for diblock copolymer melt[6] and for the multiblock one under consideration in this paper have, indeed, the opposite signs, which just corresponds to distinction between the inversed and direct morphologies.

It is easy to check that the same rule holds for the bcc phase: The A- and B-micelles are formed in the BCs with $\gamma < 0$ and $\gamma > 0$, respectively. We conclude that in the multiblock copolymers studied in this paper the longer tails segregate into the minority phase (micelles, infinite cluster, etc.) in all morphologies such as the HEX, bcc, and G whose reciprocal lattice contains regular triangles of vectors.

B. Free energies and phase diagram

The free energies per unit volume of the ordered phases and, thus, the phase diagram are calculated within the rectangle

$$\Pi = \{(f, \chi N): 0.39 \leq f \leq 0.61, \quad 9 \leq \chi N \leq 13\}. \quad (50)$$

Obviously, due to the structure symmetry of the system under investigation with respect to the exchange $f \Leftrightarrow 1-f$, $A \leftrightarrow B$, it is sufficient to build the phase diagram in the half of the region (50), for definiteness, for $0.39 \leq f \leq 0.5$.

The spinodal $\chi N_{sp}(f)$, which defines the region where the spatially uniform state of our system stays stable with respect to infinitesimal fluctuations of the order parameter (at least, metastable), is calculated within the random phase approximation.[24,25] Within the region (50), the spinodal values satisfy the inequality $9.23 < \chi N_{sp}(f) < 9.33$. The solutions of the SCFT equations are found on the grid $\chi N_{sp}(f) < \chi N \leq 13$ with an increment $\Delta \chi N = 0.02$ of 0.02 and $f = 0.5 - 0.01k$ ($k=0, 1, \ldots, 11$). To find out the morphology with the minimal free energy (i.e., the actually stable rather than only metastable symmetry), the values of the free energy for each symmetry candidate (LAM, HEX, fcc, bcc, $Fddd$, and G) have been calculated.[62] In general, the differences $\Delta F_\alpha = F_\alpha - F_{bcc}$ between the free energies ($\alpha = $ HEX,
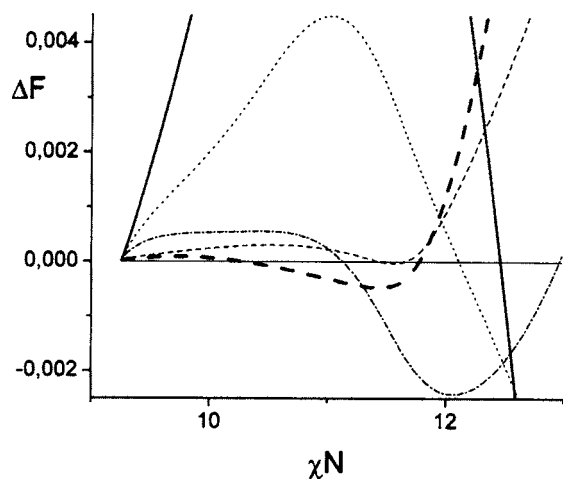
FIG. 7. The free energy differences $F_\alpha - F_{bcc}$ at $f = 0.44$ as the functions of the χN parameter for α=LAM (bold solid); α=fcc (bold dashed); α=G (dotted), α=Fddd (thin dashed), α=bcc (thin solid), and α=HEX (dash-dotted) curves.

FIG. 9. The reduced (by the radius of gyration) periods of the stable morphologies as functions of the reduced Flory–Huggins parameter χN at $f = 0.44$. The parts of the curves corresponding to the stable and metastable phases are plotted by the bold solid and thin dashed lines, respectively, the dotted lines are the guides for eyes demarcating the boundaries between the stable phases.

fcc, G, LAM, Fddd) are shown in Fig. 7 as functions of χN for $f = 0.44$, the corresponding plot for the bcc phase itself being just the x-axes. As is seen from Fig. 7, the intervals of the different phases' stability are here as follows: bcc ($9.26 < \chi N < 10.28$), fcc ($10.28 < \chi N < 11.29$), HEX ($11.29 < \chi N < 12.49$), G ($12.49 < \chi N < 12.59$), and LAM ($\chi N > 12.59$). Both here and in other points of the described grid, the orthorhombic phase Fddd is never found to be dominant. Combining similar data for all values of the tails' asymmetry parameter f, we get the phase diagram shown in Fig. 8, which is the main result of our calculations.

The bold solid lines are those of the OOT and ODT between the absolutely stable morphologies (symmetries) calculated via the SCFT procedure described above whereas the dashed lines are those calculated within WST.[24] As seen from Fig. 8, in the vicinity of the critical point $f = 0.5$, $\chi N = 9.23$ (the right bottom corner of Fig. 12) the SCFT and WST phase transition lines approach each other and merge finally in the very critical point, as expected. However, there
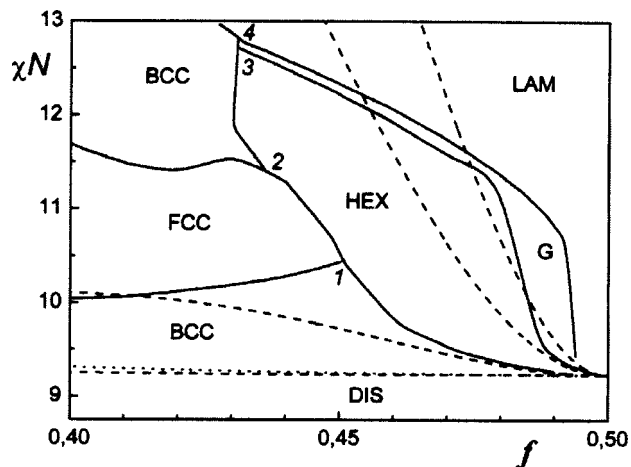
is a considerable quantitative difference between the predictions of these two theoretical approaches, the more the state of the system is remote from the critical point the bigger is the difference. It is worth to note that the SCFT phase diagram shown in Fig. 8 contains four triple points $(f, \chi N)$ where three phases are in equilibrium: bcc-fcc-HEX (0.45, 10.45), bcc-fcc-HEX (0.435, 11.42), bcc-G-HEX (0.43, 12.71), and bcc-G-LAM (0.43, 12.83).

Now, in a large (right) part of the phase diagram, the temperature sequence of the SCFT phase transition lines is DIS-bcc-HEX-G-LAM in agreement with the WST theory.[24,25] However, in the left part of the phase diagram, we observe two completely new features, which are not predictable by the WST: There is a big region of the fcc phase stability and the re-entrant phase transition fcc-bcc with increasing of χ (in the left corner of the phase diagram). It could be useful to note that, as shown in Fig. 11, the fcc phase is formed from almost spherical domains, which are filled by the long end block and arranged on the fcc lattice.

C. χ (temperature) dependence of the periodicity

To describe the stable morphology fully, we are to determine not only its symmetry but also the period L of the corresponding lattice. Whereas the WST provides only the wave number value characterizing the critical harmonic composition fluctuations destroying stability of the spatially uniform state on the spinodal, the SCFT makes it possible to calculate L at any degree of segregation. The dependences $L(\chi N)$ are shown for both stable and metastable phases for $f = 0.44$ in Fig. 9. The values of the periods L of the conventional phases LAM, HEX, and bcc as well as G converge to the WST value $L^* = 2\pi/q^*$ near the spinodal. It is worth to note the unusually high value of $L(\chi N)$ for the fcc phase, which, actually, is never stable within the region where the WST is applicable. We discuss the reasons for this exceptional behavior below.

As is seen from Fig. 9, within the region (50) studied in this paper, the periods of all phases decrease with increasing

FIG. 8. Phase diagram for the BC system $n = 3$, $m = 2$. The solid and dashed lines correspond to the SCFT and WST phase transition lines, respectively. The triple points are numbered in ascending order of the corresponding χ values.
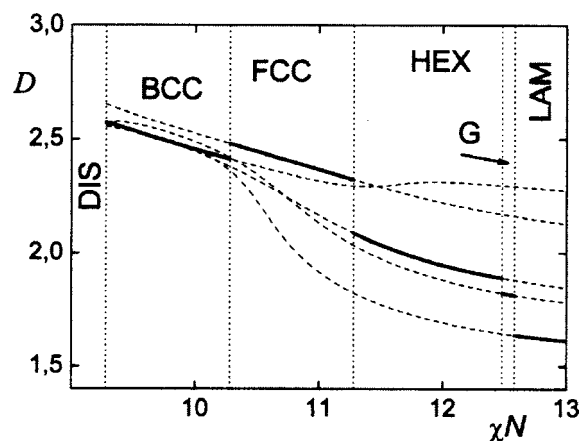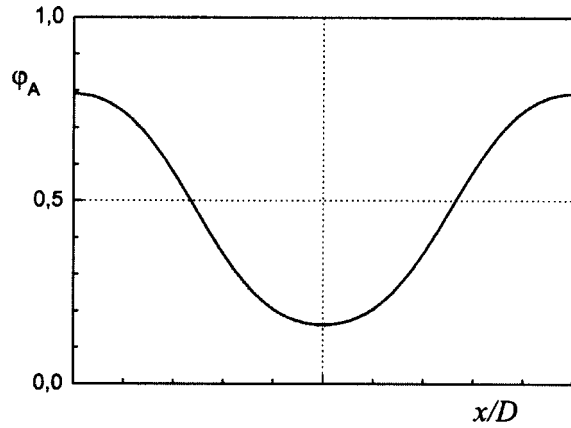
FIG. 10. The one-dimensional distribution of the total volume fraction $\varphi_A(\mathbf{r})$ for the lamellar phase at the triple point 4.

FIG. 12. (Color) The 3D distribution of the total volume fraction $\varphi_A(\mathbf{r})$ for the G morphology at the triple point 4. The color legend is the same as in Fig. 3 but the particular values of φ_A assigned to the limiting colors.

incompatibility (and, thus, segregation) in contrast to the typical increase of the period L with χN for AB diblock copolymers. The case is that whereas the tails of the multiblock macromolecule $A_{fmN}-b-(B_{N/2}-b-A_{N/2})_n-b-B_{(1-f)mN}$ under investigation are expected to stretch and "polarize" with χN as was shown to be the case for the blocks of diblock macromolecule,[65,66] the middle part of the macromolecule shrinks to adjust to the segregation conditions, which is evidenced by the fact that the values of q^* are smaller (and, thus, the period L larger) in the diblock copolymers than in periodic multiblocks made of the same diblocks.[67,68] We address this effect in much more details in our work[69] devoted to the analysis of the lamellar-in-lamellar structure. According to the presented SCFT results, it is this shrinking that determines the final temperature dependence $L(\chi N)$.

D. The composition distributions in the direct and Fourier space and their temperature (χ) dependence

The spatial distributions of the volume fraction $\varphi_A(\mathbf{r})$ of A monomers for the parameters $(f, \chi N)$ close to the triple points of the phase diagram 12 were calculated and some of them were already presented in Figs. 3–5. It has been shown that to visualize these data is not a trivial task and requires many images. Some additional pictures are presented in Figs. 10–12 for the lamellar, fcc, and gyroid phases. It is worth to mention the clear meander motif rather the characteristic of the double gyroid, which is seen in Fig. 12, and the fact that the composition profile is rather smooth (no narrow inter-
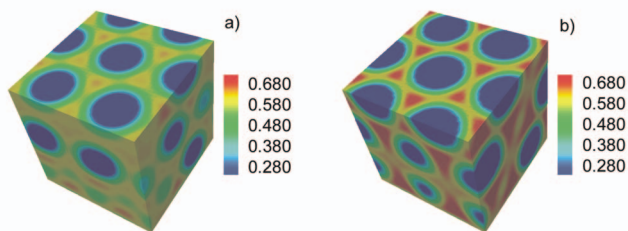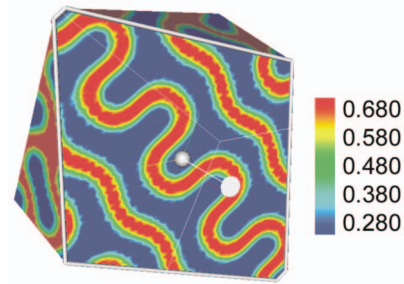

FIG. 11. (Color) The 3D distributions of the total volume fraction $\varphi_A(\mathbf{r})$ for the fcc morphology at the triple points 1 (a) and 2 (b). The color legend is the same as in Fig. 3 but the particular values of φ_A assigned to the limiting colors.

face) even though the segregation degree is quite considerable already as is revealed by the lamellar profile shown in Fig. 10. The 3D pictures shown in Figs. 5, 11, and 12 are nice but they would considerably change if the point of origin moves or the axes rotate as is seen partly in Fig. 12. Even more problems would arise when attempting to visualize continuous morphology changes with temperature. At last, the computer 3D visualization could be even misleading. For example, the G phase in Fig. 12 seems to have rather well defined interfaces whereas, in fact, the latter are rather smooth as is clearly seen from the LAM phase profile shown in Fig. 10 at the same degree of segregation. Therefore, to have an adequate idea of spatial distributions for various morphologies and their temperature evolution, it is natural to look for some invariant data.

Such invariant data are just the harmonics spectra, i.e., the sets of the values $\{a_m = |A_m|\}$ of the Fourier harmonics amplitudes present in the Fourier series

$$\Delta(\mathbf{r}) = \sum_{q_i} (A_{q_i} \exp i(\mathbf{q}_i \mathbf{r} + \phi_i) + \text{c.c.}),$$

which are to be found anyway as some by-products under calculation of $\varphi_A(\mathbf{r})$. Moreover, it is the spectrum of the volume fraction $\varphi_A(\mathbf{r})$ rather than its 3D visualization, which provides the unambiguous identification of the morphology. The third important advantage of studying the spectra is that it gives valuable information on the observable peak intensities of the small-angle scattering with the scattering vector $\mathbf{q}_m$, which are proportional to $|A_{\mathbf{q}_m}|^2$. The temperature behavior of the amplitudes A_{q_m} at $f = 0.44$ for studied morphologies is plotted in Fig. 13. The curves are classified by the rational value of the reduced square of the corresponding coordination sphere $h = q_m^2/q_*^2$. We refer to the harmonics with $h = k^2$ and $(k-1)^2 < h \leq k^2$ as the multiple, and belonging to the kth shell, respectively.

First, we notice that the saw tooth part of the curve corresponding to the weakest harmonics (the seventh) at the very onset of microphase separation for the LAM morphology gives an idea of the inaccuracy involved in our calculations and, thus, justifies all the data with $A > 1 \times 10^{-7}$. One of the most remarkable features seen from Fig. 12 is that only few harmonics (including the dominant one) monotonously
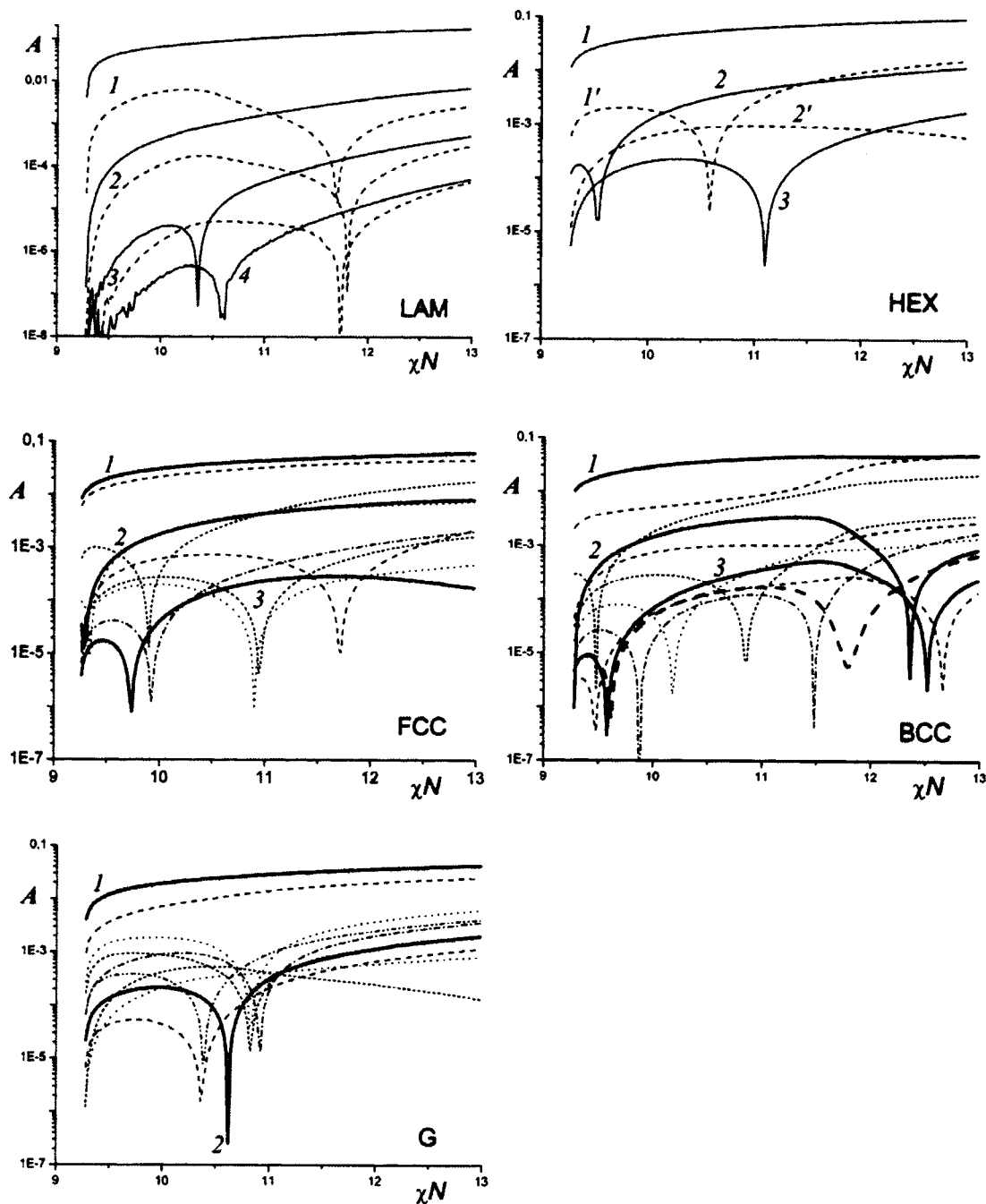
FIG. 13. The χ dependence of the volume fraction $\varphi_A(\mathbf{r})$ spectra at $f=0.44$ for the LAM, HEX, fcc, bcc, and G morphologies. (LAM) the odd and even harmonics are plotted by the solid and dash lines, respectively, the odd $[h=(2k-1)^2]$ and even $[h=(2k)^2]$ harmonics are labeled by the number k; (HEX) the multiple $(h=1,4,9)$ and higher $(h=3,7)$ harmonics are plotted by the solid and dash lines, respectively, and labeled by the numbers of their shell. For fcc, bcc, and G the multiple harmonics are plotted by the bold solid lines and labeled by the numbers of their shell. The higher harmonics are plotted by (i) the dash $(h=4/3,16/3)$, short dash $(h=8/3,19/3)$, dot $(h=11/3,20/3)$, and dash dot $(h=8)$ lines for fcc; (ii) dash $(h=2,5,10)$, short dash $(h=3,6)$, dot $(h=7)$, dash dot $(h=8)$, and bold dash (for $\mathbf{m}=(\pm4,\pm1,\pm1)$ with $h=9$) lines; (iii) dash $(h=4/3,13/3)$, short dash $(h=7/3,16/3)$, dot $(h=8/3,8)$, dash dot $(h=10/3)$, and dash dot dot $(h=11/3)$ lines for G. To not overload the figures, the higher harmonics are not labeled. They are easily recognized since their strength noticeably decreases with increase of the shell number.

increase when segregation increases. Most of the higher harmonics reveal rather pronounced dips (sometimes multiple) clearly evidencing that these harmonics vanish at some temperature and then increase again. One can state that nonmonotonous temperature dependence and even vanishing and reappearance of the secondary peak scattering intensities is rather a rule than exception. A remarkable property of the LAM phase is that all even harmonics vanish within a rather

narrow χ interval. At the moment, we cannot explain this behavior; it should be considered as a sort of experimental finding.

Interesting information is provided by the spectrum of the fcc and G phases, where the strength of the second harmonics with $h_m=|\mathbf{q}_m|^2/q_*^2=4/3$ is comparable to that of the dominant one. This effect is known for the G phase,[70] but it is even more pronounced for the fcc phase. It is strongly

different from the WST predictions for diblock[6] and *ABC* triblock[23] copolymers, where the harmonics with $h_m = 4/3$ would be missing in the fcc morphology. The case is that within the first harmonics approximation (42) the minimum of the free energy F_{fcc} is provided[6] by such a choice of the phases ϕ_i, which, unlike that found in our SCFT calculations, results in full suppression of the harmonics with $h_m = 4/3$. Thus, in contrast to the conventional morphologies LAM, HEX, bcc, where all the higher harmonics in the conventional morphologies LAM, HEX and bcc are small as compared to the main harmonics within a noticeable interval of the χ values, the first harmonics approximation (33) is completely inadequate for the fcc and rather inadequate for the G phases.

IV. CONCLUSION

In summary, in this paper, we presented the SCFT analysis of the phase diagram for the two-length scale architecture multiblock copolymers $A_{fmN}(B_{N/2}A_{N/2})_n B_{(1-f)mN}$ with $m=2$ and $n=3$, in which case the phase transition sequence predicted within the WST is DIS-bcc-HEX-G-LAM.[24] We applied the pseudospectral method to solve the modified diffusion equation with periodical conditions and proposed a new, more exact, discrete approximation for the operator $\exp(-\Delta s \nabla^2)$. Our algorithm provides a fast convergence and a high precision of the solution, 3D symmetries being calculated in a reasonable computer time due to using (i) the Ng iterations,[55] (ii) a special choice of the predefined symmetries of the computation cell, and (iii) the proper symmetry information input in the initial iteration taken from the WST.

We focus on the region of not too high values of the χ-parameter, where segregation inside the middle multiblock part $(B_{N/2}-b-A_{N/2})_3$ does not occur yet and, thus, the system phase behavior is somewhat similar to that of the ternary linear *ABC* block copolymers with the middle block *B* nonselective with respect to the side blocks *A* and *C*. The sequence of the phase transitions found previously within the WST holds for not too asymmetric tails of the BCs under consideration ($0.45 \leq f_A \leq 0.5$) but the quantitative agreement between the WST and SCFT phase diagrams is reasonable in a rather narrow (both in f and $\tilde{\chi} = \chi N$) region close to the critical point. Another qualitative WST-based prediction (the fcc phase stability found[24] for architectures with somewhat different values of n and m than discussed in the present work or extended beyond the WST applicability region) is also confirmed by our SCFT calculations. Namely, for $f_A \leq 0.45$, a large region of the fcc stability is found via the SCFT calculations inside of that of the bcc lattice. It is worth to note that in the previous SCFT treatments[16,43,44] of the *ABC* BC melts the fcc phase was not reported. This discrepancy could be both due to the trivial absence of the fcc phase in the list of the plausible candidates to the stable morphologies in Refs. 16, 43, and 44 and because of the actual difference in the phase behavior of the genuine ternary *ABC* BCs and that of our *ABC*-like but, actually, *AB* multiblock ones. The latter option is somewhat supported by the fact that the *Fddd* phase found to be stable at some compo-

sitions of the *ABC* BCs (Refs. 43 and 44) is always metastable for multiblock copolymers studied in the present paper.

A new phenomenon, which is occurrence of the inversed two-dimensional (2D) and 3D phases with the micelles formed, in contrast to the conventional diblock copolymers, by the longer rather than shorter tails, and its relationship to the BC architecture are first described in detail. We expect the inversed morphologies to have various applications and occur in many other copolymer systems. In particular, as suggested by Khokhlov, the inversed morphologies could be expected in BCs with amphiphilic monomers.

[1] F. S. Bates and G. H. Fredrickson, Annu. Rev. Phys. Chem. **41**, 525 (1990).
[2] I. Ya. Erukhimovich and A. R. Khokhlov, Polym. Sci., Ser. A **35**, 1522 (1993).
[3] K. Binder, Adv. Polym. Sci. **112**, 181 (1994).
[4] F. S. Bates and G. H. Fredrickson, Phys. Today **33**(52), 32 (1999).
[5] F. S. Bates, MRS Bull. **30**, 525 (2005).
[6] L. Leibler, Macromolecules **13**, 1602 (1980).
[7] I. Ya. Yerukhimovich, Polym. Sci. U.S.S.R. **24**, 2223 (1982).
[8] K. M. Hong and J. Noolandi, Macromolecules **16**, 1083 (1983).
[9] A. N. Semenov, Sov. Phys. JETP **61**, 733 (1985).
[10] A. M. Mayes and M. Olvera de la Cruz, J. Chem. Phys. **91**, 7228 (1989).
[11] A. V. Dobrynin and I. Ya. Erukhimovich, Macromolecules **26**, 276 (1993).
[12] M. W. Matsen and M. Schick, Phys. Rev. Lett. **72**, 2660 (1994).
[13] M. W. Matsen and M. Schick, Macromolecules **27**, 6761 (1994).
[14] M. W. Matsen, Phys. Rev. Lett. **74**, 4225 (1995).
[15] M. W. Matsen and F. S. Bates, Macromolecules **29**, 1091 (1996).
[16] M. W. Matsen, J. Chem. Phys. **108**, 785 (1998).
[17] G. H. Fredrickson, *The Equilibrium Theory of Inhomogeneous Polymers* (Oxford University Press, New York, 2006).
[18] *Supramolecular Polymers*, edited by A. Ciferri (Dekker, New York, 2000).
[19] *Block Copolymers in Nanoscience*, edited by M. Lazzari, G. Liu, and S. Lecommandoux (Wiley-VCH, New York, 2006).
[20] *Nanostructured Soft Matter: Experiment, Theory, Simulation and Perspectives*, NanoScience and Technology, edited by A. V. Zvelindovsky (Springer, New York, 2007).
[21] D. A. Hajduk, P. E. Harper, S. M. Gruner, C. Honeker, G. Kim, and E. L. Thomas, Macromolecules **27**, 4063 (1994).
[22] S. Forster, A. K. Khandpur, J. Zhao, F. S. Bates, I. W. Hamley, A. J. Ryan, and W. Bras, Macromolecules **27**, 6922 (1994).
[23] I. Y. Erukhimovich, Eur. Phys. J. E **18**, 383 (2005).
[24] Yu. G. Smirnova, G. ten Brinke, and I. Ya. Erukhimovich, J. Chem. Phys. **124**, 054907 (2006).
[25] Yu. G. Smirnova, G. ten Brinke, and I. Ya. Erukhimovich, J. Polym. Sci. A **47**, 740 (2005).
[26] I. Erukhimovich, in Proceedings of the International Conference on Advanced Polymers and Processing ICAPP 2001 Yonezawa, Japan, edited by K. Iwakura pp. 122–128.
[27] Y. G. Smirnova (unpublished) Ph.D. thesis, Rijksuniversiteit Groningen, 2006.
[28] J. Ruokolainen, R. Mäkinen, M. Torkkeli, T. Mäkelä, R. Serimaa, G. ten Brinke, and O. Ikkala, Science **280**, 557 (1998).

29 J. Ruokolainen, G. ten Brinke, and O. Ikkala, Adv. Mater. (Weinheim, Ger.) **11**, 777 (1999).

30 O. Ikkala and G. ten Brinke, Science **295**, 2407 (2002).

31 Y. Nagata, J. Masuda, A. Noro, D. Cho, A. Takano, and Y. Matsushita, Macromolecules **38**, 10220 (2005).

32 J. Masuda, A. Takano, Y. Nagata, A. Noro, and Y. Matsushita, Phys. Rev. Lett. **97**, 098301 (2006).

33 C. M. Hardy, F. S. Bates, M.-H. Kim, and G. D. Wignall, Macromolecules **35**, 3189 (2002).

34 R. Nap, C. Kok, G. ten Brinke, and S. Kuchanov, Eur. Phys. J. E **4**, 515 (2001).

35 R. Nap and G. ten Brinke, Macromolecules **35**, 952 (2002).

36 I. Erukhimovich, Y. Smirnova, and V. Abetz, Polym. Sci., Ser. A **45**, 1093 (2003).

37 E. W. Cochran, D. C. Morse, and F. S. Bates, Macromolecules **36**, 782 (2003).

38 R. Nap, I. Erukhimovich, and G. ten Brinke, Macromolecules **37**, 4296 (2004).

39 S. Tarasenko and I. Erukhimovich, Polym. Sci., Ser. A **47**, 229 (2005).

40 R. Nap, N. Sushko, I. Erukhimovich, and G. ten Brinke, Macromolecules **39**, 6765 (2006).

41 S. Tarasenko and I. Erukhimovich, Polym. Sci., Ser. A **48**, 207 (2006).

42 S. Kuchanov, V. Pichugin, and G. ten Brinke, Europhys. Lett. **76**, 959 (2006).

43 C. A. Tyler and D. C. Morse, Phys. Rev. Lett. **94**, 208302 (2005).

44 C. A. Tyler, J. Qin, F. S. Bates, and D. C. Morse, Macromolecules **40**, 4654 (2007).

45 F. Drolet and G. H. Fredrickson, Phys. Rev. Lett. **83**, 4317 (1999).

46 J. G. E. M. Fraaije, J. Chem. Phys. **99**, 9202 (1993).

47 N. M. Maurits and J. G. E. M. Fraaije, J. Chem. Phys. **107**, 5879 (1997).

48 A. Subbotin, T. Klymko, and G. ten Brinke, Macromolecules **40**, 2915 (2007).

49 E. Helfand and Z. R. Wasserman, in *Developments in Block Copolymers*, edited by I. Goodman (Applied Science, London, 1982), p. 99.

50 E. Helfand and Z. R. Wasserman, Macromolecules **9**, 879 (1976).

51 M. W. Matsen, Phys. Rev. Lett. **74**, 4225 (1995).

52 M. D. Feit, J. A. Fleck, and A. Steiger, J. Comput. Phys. **47**, 412 (1982).

53 K. O. Rasmussen and G. Kalosakas, J. Polym. Sci., Part B: Polym. Phys. **40**, 1777 (2002).

54 H. D. Ceniceros and G. H. Fredrickson, Multiscale Model. Simul. **2**, 452 (2004).

55 K.-C. Ng, J. Chem. Phys. **61**, 2680 (1974).

56 R. B. Thompson, K. Ø. Rasmussen, and T. Lookman, J. Chem. Phys. **120**, 31 (2004).

57 G. H. Fredrickson, V. Ganesan, and F. Drolet, Macromolecules **35**, 16 (2002).

58 *International Tables for Crystallography* (Kluwer, Dortdrecht, 1996), Vol. B.

59 G. E. Forsyte, M. A. Malcolm, and C. B. Moler, *Computer Methods for Mathematical Computations* (Prentice-Hall, Englewood Cliffs, NJ, 1977).

60 I. Ya. Erukhimovich, *Nanostructured Soft Matter: Experiment, Theory, Simulation and Perspectives*, Nanoscience and Technology, edited by A. V. Zvelindovsky (in Ref. 20), Chap. 11.

61 A noise seen in our morphology plots is related to the visualization program (public software PARAVIEW) we used rather than due to the lack of convergence (see also discussion of Fig. 13).

62 We have not included into our consideration the symmetries corresponding to perforated lamellar (PL) morphologies not only because there are only very few exceptions when the PL are found to be dominant (Ref. 63). The change in architecture might, in general, cause the PL stability, but the preliminary WST analysis, in which we use the WST description of the PL as an underlying hexagonal-close-packing (HCP) lattice (Ref. 64) does not support this option for the multiblock copolymers under consideration. We present this analysis in more details elsewhere.

63 M. W. Matsen, Macromolecules **28**, 5765 (1995).

64 S. Y. Qi and Z.-G. Wang, Phys. Rev. E **55**, 1682 (1997).

65 I. Ya. Erukhimovich and A. V. Dobrynin, Macromolecules **25**, 4411 (1992).

66 J. L. Barrat and G. H. Fredrickson, J. Chem. Phys. **95**, 1281 (1991).

67 I. Ya. Yerukhimovich, Polym. Sci. U.S.S.R. **24**, 2232 (1982).

68 H. Benoit, G. Hadziioannou, Macromolecules **21**, 1449 (1988).

69 Yu. A. Kriksin, I. Ya. Erukhimovich, P. G. Khalatur, Yu. G. Smirnova, and G. ten Brinke, *A non-monotonous dependence of the lamellar-in-lamellar structure in binary linear multiblock copolymers on their architecture and temperature* (submitted).

70 I. W. Hamley and V. E. Podnek, Macromolecules **30**, 3701 (1997).